In-situ coupling Co-Mo bimetallic sulfide derived from $[CoMo_{12}O_{40}]^{6-}$ cluster showing highly efficient electrocatalytic hydrogen evolution

Qingfang Zhen[a], Haijun Pang[a], Sumin Hu[a], Zhongxin Jin[a], Qiong Wu[b], Huiyuan Ma*[a],*

Xinming Wang[a], Guixin Yang[a] and Zhipeng Yu[c]*

[a]School of Materials Science and Chemical Engineering, Harbin University of Science and Technology, Harbin, 150040, P. R. China
[b]Department of Chemical Science and Technology, Kunming University, Kunming, Yunnan, 650214, China.
[c]Clean Energy Cluster, International Iberian Nanotechnology Laboratory (INL), Avenida Mestre Jose Veiga, 4715-330 Braga, Portugal

**E-mail:* panghj116@163.com, mahy017@163.com, zhipeng.yu@inl.int

Table of Contents

Section 1 Additional Experimental Section

I. Materials and General Methods

All reaction reagents are commercially available and can be used without further purification. The reagents used in the experiments were $H_4PMo_{12}O_{40}\cdot 3H_2O$, $Co(NO_3)_2\cdot 6H_2O$, CH_3COONa, $Co(CH_3COO)_2\cdot 4H_2O$, and imidazole. FI-IR spectra were recorded from KBr particles in the 4000-400 cm^{-1} range using a Bruker OPTIK GmbH-Tensor II spectrometer. Crystallographic data were collected at room temperature using a Bruker SMART APEX II single crystal X-ray diffractometer with Mo Kα radiation. Data were parsed using SHELXTL 97 software and refined using the least squares F^2 method. X-ray powder diffraction (XRPD) patterns were obtained using an X'Pert-Pro MPD diffractometer at 25 °C and Cu-Kα radiation at a scan rate of 5°/min and a 2θ range of 10° to 80°. X-ray photoelectron spectroscopy (XPS) measurements were performed using a Thermo ESCALAB 250Xi spectrometer with monochromatic Al K_α radiation (hγ = 1486.6 eV). All XPS spectra are corrected by a C 1s peak at 284.8 eV.

The morphology of the samples was analyzed using scanning electron microscopy (SEM, SIGMA300) and transmission electron microscopy (TEM, JEM-F200). Both cyclic voltammetry (CV), linear sweep voltammetry (LSV) tests, current density *vs* time (I-t) curves and electrochemically active surface area (ECSA) were conducted with a CHI760E workstation in a conventional three electrode system, The MoS_2/CoS_2/CC series electrodes (S = 1 cm^2) served as the working electrode in electrochemical experiments, and a saturated calomel electrode (SCE) as the reference electrode. And, graphite rod was considered as counter electrode. All the final potentials were expressed in reference to the reversible hydrogen electrode (RHE) via the Nernst equation: in 1.0 M KOH, $E_{RHE} = E_{SCE} + 1.07$ V. Linear sweep voltammetry (LSV) is conducted from -1.0 to 0 V with a scan rate of 5 mV s^{-1} for HER. A steady N_2 flow was used to remove hydrogen gas bubbles formed at the catalyst surface. The durability tests were carried out by repeating the potential at a scan rate of 100 mV s^{-1} for 2000 cycles. All current densities are the ratios of currents and geometric areas of working electrodes. The ECSA was elucidated by measuring double layer capacitance (C_{dl}) of cyclic

voltammetry (CV) at non-Faradaic potentials (-0.25 – -0.05 V in 1.0 M KOH *vs* RHE, respectively) recorded at different scan rates from 10 to 100 mV s^{-1}. The electrochemical impedance spectroscopy (EIS) measurement was measured in the frequency range from 0.005 Hz to 100 kHz.

II. Synthesis of $CoMo_{12}$:

According to the literature [1], $Na_2MoO_4 \cdot 2H_2O$ (1.245 g, 5 mmol) and CH_3COONa (0.5 g, 6 mmol) were dissolved in 20 mL distilled water, and then 0.238 g (0.83 mmol) of $Co(CH_3COO)_2 \cdot 4H_2O$ was added. Stir the solution for 10 min, then add 0.225 g (3.3 mmol) imidazole. Then adjust from 85% acetic acid to a pH of 4.6 to 4.8 to form a deep red color. The solution was stirred at 55 to 60 °C for reflux for about 3 hours, then cooled to room temperature and filtered into a 50 mL beaker (the final pH of the solution was still in the 4.6 to 4.8 range). After a few days, the purple powder is polyoxometalate $(C_3H_5N_2)_6[Co^{II}Mo_{12}O_{40}] \cdot 10H_2O$.

III. Synthesis of CoS_2-CC composites:

A drop of polytetrafluoroethylene (PTFE) binder solution was dropped into a certain amount of polyoxometalate, then 2 mL ethanol solution was added, and ultrasonic treatment was conducted for 30 min, and the above solution was put into the oven at 60℃ to dry. A piece of CC with an area of 1x1.5 cm^2 was cut out, and the dried material was evenly coated on both sides of CC. $CoMo_{12}$-CC material was successfully prepared

IV. Synthesis of MoS_2/CoS_2/CC composites:

A reaction solution was prepared by $CoMo_{12}$ polyoxometalate, 0.06 g of thiouurea (TU) and 10 mL of deionized water. Added a piece of CC with an area of 1 × 1.5 cm^2 and stirred at room temperature for 1.5 hours. Then the reaction solution was transferred to a PTFE reactor and kept at 200 °C for 24 hours. Then washed and dried.

V. Infrared characterization of cobalt-polyoxometalate:

The prepared $CoMo_{12}$ polyoxometalate was characterized by Fourier infrared spectroscopy. The stretching vibration peaks of Mo=O appeared at 963 cm^{-1} and 874 cm^{-1}, and the wave numbers corresponding to bending vibration peaks of Mo-O-Mo were 548 cm^{-1}, 626 cm^{-1} and 792 cm^{-1} as shown in Fig. S1. The characteristic absorption

peaks at 3452 cm^{-1} and 1622 cm^{-1} were generated by the O-H stretching vibration of water molecules, and the characteristic absorption peaks of Keggin-type polyoxometalate anions appeared at 1000 - 600 cm^{-1}, which were consistent with the position of the peaks in the literature [2]. The synthesis of $CoMo_{12}$ polyoxometalates was preliminarily proved.

VI. X-ray photoelectron spectroscopy

XPS survey spectra of MoS_2/CoS_2/CC composites were shown in Fig. S2. It could be seen from the figure that typical characteristic peaks appeared at 232.4 and 233.2eV, which were respectively attributed to Mo^{4+} $3d_{5/2}$ and Mo^{4+} $3d_{3/2}$, which were typical characteristic peaks of MoS_2. S 2p had several groups of characteristic peaks, which were S $2p_{3/2}$ (161.6eV), S $2p_{1/2}$ (163.3eV), S-C (164.2eV) and SCN^- (160.6eV). Therefore, four characteristic peaks appeared at 796.7, 797.5, 782.1 and 779.5 eV, which were attributed to Co^{2+} $2p_{3/2}$, Co^{2+} $2p_{1/2}$, Co^{3+} $2p_{3/2}$ and Co^{3+} $2p_{1/2}$, respectively. In addition, the characteristic peaks at 802.1 and 787.7 eV were attributed to the satellite peaks of Co 2p. It further proved the elemental composition and valence state of the material.

VII. Energy Dispersive Spectroscopy:

It was shown in Fig. S3 that the atomic ratio of Co to Mo was about 1:12, which was consistent with the atomic ratio in the precursor $CoMo_{12}$ polyoxometalate.

VIII. Electrochemical impedance test:

In addition, the EIS measurements were also carried out on the two composites. There was no obvious semicircle in the high frequency region of Nyquist diagram of MoS_2/CoS_2/CC composite electrodes, so the intersection point between the curve and the real axis in Nyquist diagram represented the ohmic impedance of the electrode materials. It also represented the electron conductivity of the materials. As shown in Fig. S4, it was the EIS spectrum of MoS_2/CoS_2/CC composites under different pH conditions, reaction times, reaction temperatures and Mo/S ratios. It could be observed that the curve slope of MoS_2/CoS_2/CC composites was higher in the low frequency region of EIS spectrum, when the reaction time was 24 h, the reaction temperature was

200℃ and Mo/S = 1:4 in the EIS spectrum, so its resistance was lower under this reaction condition, and its ion diffusion ability was stronger.

IX. Measurements of PXRD pattern and SEM before and after the reaction:

The PXRD pattern before and after the reaction was used to further verify the electrode stability. As shown in Fig. S5, the electrode materials which had been electrochemical tested were tested by PXRD. Obviously, the diffraction peaks of the material did not change strongly, and the diffraction peaks coincided in height, indicating that the material phase did not change, before and after the electrocatalytic hydrogen evolution tests. It also proved once again that MoS_2/CoS_2/CC composites had excellent electrochemical stability.

Moreover, the SEM image before and after the reaction is shown in Fig. S6. It can be found that there is no significant morphology change in the material before and after the reaction.

Section 2 Supplementary Figures

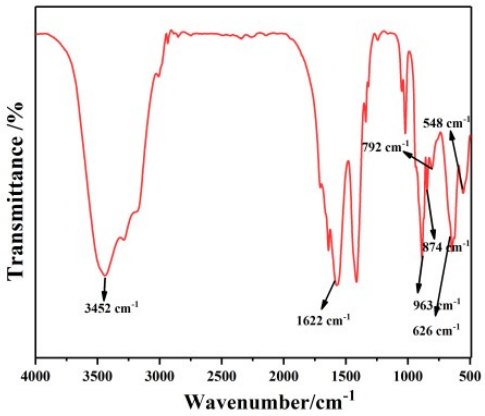

Fig. S1. The IR spectrum of compound of $CoMo_{12}$.

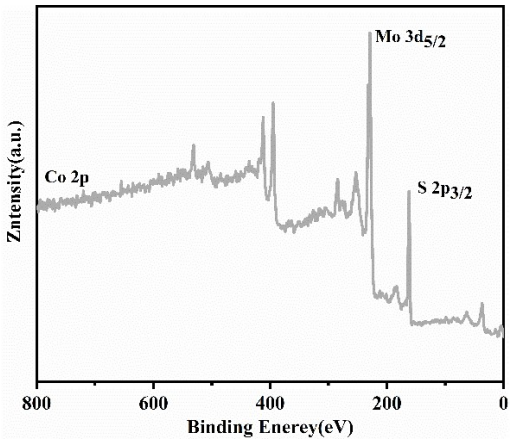

Fig. S2 XPS spectrum of $MoS_2/CoS_2/CC$

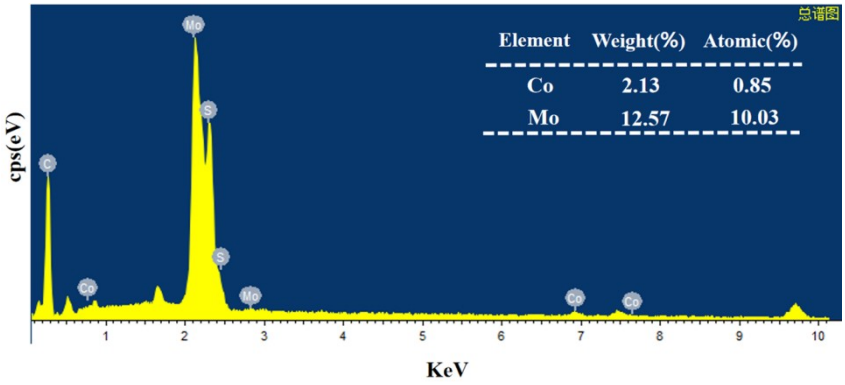

Fig. S3. EDS spectrum of $MoS_2/CoS_2/CC$.

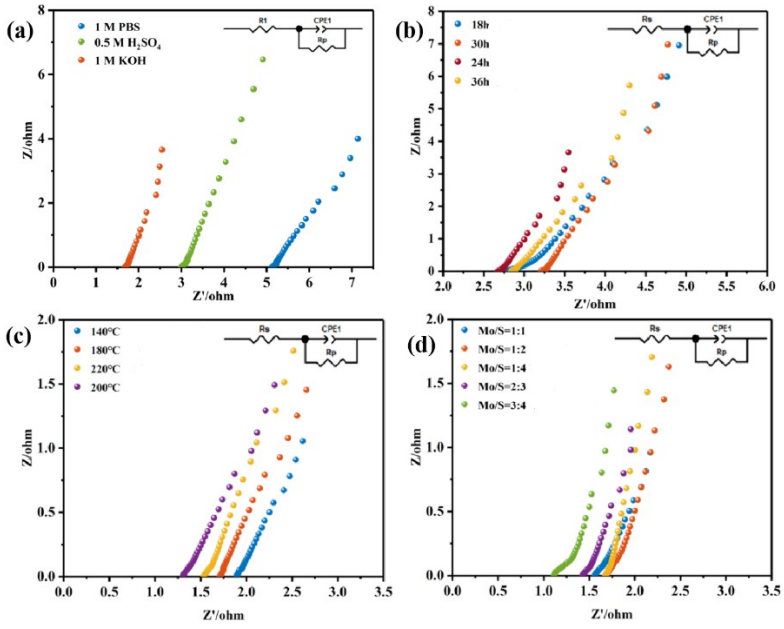

Fig. S4 EIS of $MoS_2/CoS_2/CC$: a) Different pHs, b) Different reaction times, c) Different reaction times, d) Different Mo/S ratios.

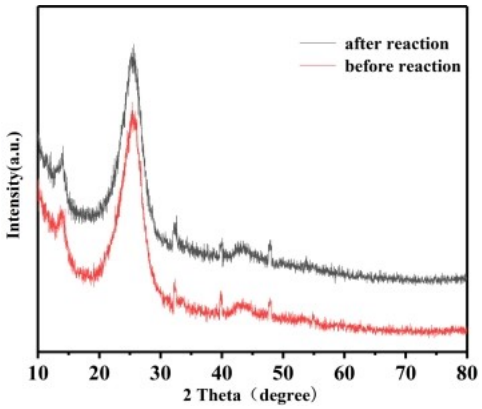

Fig. S5. PXRD plot before and after the reaction of $MoS_2/CoS_2/CC$

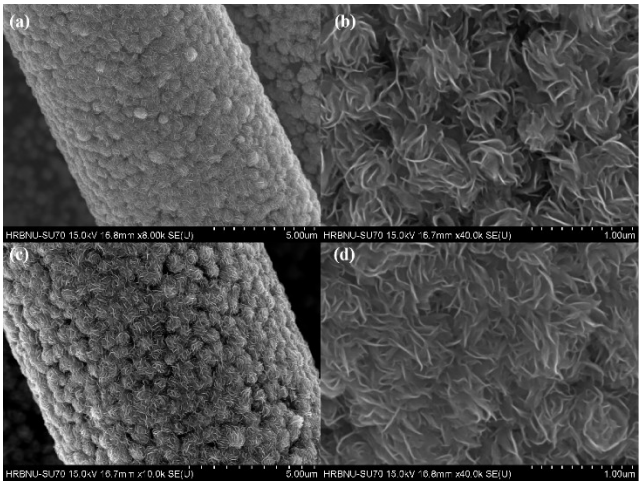

Fig. S6 SEM image before and after the reaction of $MoS_2/CoS_2/CC$: a), b) before the reaction, c), d) after the reaction.

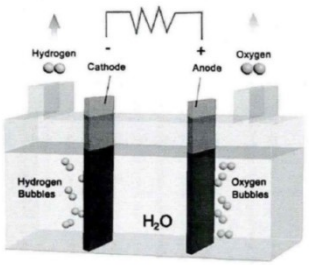

Fig. S7 A diagram shows the electron transfer during the reaction and the principle of the hydrogen precipitation reaction at the electrode

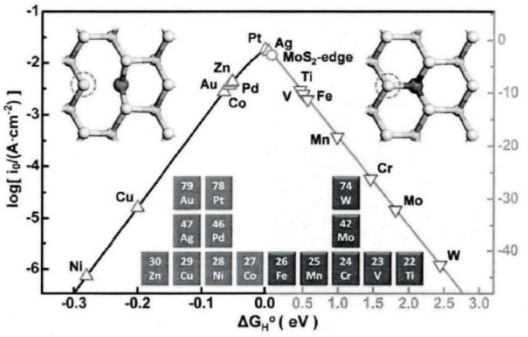

Fig. S8 Volcano plot of exchange current density as a function of Gibbs free energy for various HER catalyst materials

Section 3 Additional discussion

I. The mechanism of Mo-Co bimetallic composite act as electrode material:

Composites of bimetallic sulphides are a synergistic process with significantly improved electrochemical hydrogen precipitation performance compared to most monometallic sulphides[3]. The diagram shows the electron transfer during the reaction and the principle of the hydrogen precipitation reaction at the electrode (Fig. S7).

Electrolysis of water mainly involves the decomposition of water molecules into hydrogen and oxygen ions, followed by hydrogen and oxygen precipitation reactions at the cathode and anode respectively, consisting of two half-cell reactions. The total reaction equation for the electrolysis of water is shown below.

$2H_2O \rightarrow O_2\,(g)+2H_2\,(g)$

In both acidic and alkaline reaction electrolytes, hydrogen ions are first adsorbed on the surface of the electrocatalyst, also known as the Volmer reaction, and then the hydrogen ions adsorbed on the surface receive electrons and the re-adsorbed hydrogen ions receive electrons to produce hydrogen gas or hydrogen gas with nearby hydrogen ions that have received electrons, known as the Heyrovsky and Tafel reactions respectively. Therefore, hydrogen precipitation perovskites are divided into two types: Volmer-Heyrovsky and Volmer-Tafel reactions.

The electrocatalytic hydrogen production reaction kinetic process is shown below:

In alkaline environments:

Volmer reaction: $H_2O + e^- \rightarrow H^* + OH^-$

Heyrovsky reaction: $H^* + H^+ + e^- \rightarrow H_2$ or Tafel reaction: $H^* + H^* \rightarrow H_2$

In acidic environments:

Volmer reaction: $H^+ + e^- \rightarrow H^*$

Heyrovsky reaction: $H^* + H^+ + e^- \rightarrow H_2$ or Tafel reaction: $H^* + H^* \rightarrow H_2$

We choose to carry out electrolytic hydrogen precipitation reaction in alkaline

environment involving several processes of water decomposition, hydrogen ion adsorption and desorption, MoS_2 is less active in decomposing water molecules in alkaline environment, which is not enough to provide hydrogen ions required for hydrogen generation and becomes a hindrance in its alkaline electrolytic hydrogen precipitation reaction. The combination of CoS_2 and MoS_2 can provide sufficient hydrogen ions for the active sites at the edge of MoS_2, which can effectively reduce the potential energy of water decomposition to improve the efficiency of electrocatalytic hydrogen precipitation. Meanwhile, according to the volcano diagram (Fig. S8), we found that among the metals Co and Mo have better electrocatalytic hydrogen precipitation performance, so we chose MoS_2/CoS_2/CC as the catalyst for electrocatalytic hydrogen precipitation[4].

Section 4 References

1 G. Gao, L. Xu, W. Wang, X. Qu, H. Liu, and Y. Yang, *Inorg. Chem.*, 2008, 47(7): 2325-2333.

2 B. Lu, D. Cao, W. Pan, G. Wang, and Y. Gao, *Int. J. Hydrog. Energy*, 2011, 36(1):72-7811.

3 T. Chivers, J.B. Hyne, and C. Lau, *Int. J. Hydrog. Energy*, 1980, 5(5):499-506.

4 J. Deng, H. Li, J. Xiao, Y. Tu, D. Deng, H. Yang, H. Tian, J. Li, P. Ren and X. Bao, *Energy Environ. Sci.*, 2015, 8(5):1594-1601.